



## Supplementary Materials for

### **A mesothelium divides the subarachnoid space into functional compartments**

Kjeld Møllgård *et al.*

Corresponding authors: Kjeld Møllgård, [kjm@sund.ku.dk](mailto:kjm@sund.ku.dk); Maiken Nedergaard, [nedergaard@urmc.rochester.edu](mailto:nedergaard@urmc.rochester.edu)

*Science* **379**, 84 (2023)  
DOI: 10.1126/science.adc8810

#### **The PDF file includes:**

Materials and Methods  
Figs. S1 to S9  
Table S1  
References

#### **Other Supplementary Material for this manuscript includes the following:**

MDAR Reproducibility Checklist  
Movie S1

## Materials and Methods

### Animals

Prox1-EGFP<sup>+</sup> reporter mice kindly provided by Dr. Kari Alitalo on C57BL/6JRj background (Janvier Labs, Le Genest-Saint-Isle, France) were utilized (13). Unless otherwise stated, young Prox1-EGFP<sup>+</sup> or wildtype C57BL/6JRj of both sexes at an age of postnatal day 90-120 were used. The mice were housed in groups (4 - 5 mice per cage) with controlled temperature and humidity, on 12 hours light/dark cycles (6:00AM/6:00PM) and fed with regular rodent chow and tap water *ad libitum*. If not listed, the mice were anesthetized by intraperitoneal (i.p.) injection of a ketamine and xylazine mixture (K/X: 100 mg/kg, 20 mg/kg). Additional anesthesia (K/X: 50 mg/kg, 10 mg/kg) was administered when needed. All experiments were approved by the Animal Experiments Council under the Danish Ministry of Environment and Food (license number: 2015-15-0201-00535) and the procedures were performed in accordance with the European directive 2010/63/EU, with due care to minimize the number of animals included in the study. As a common rule for all the performed experiments, data from animals presenting bleeding or a surgical injury were excluded from the analysis. When relevant, power analysis were used to determine sample size.

### Human tissue samples

Human fetal material was obtained from legal abortions after obtaining informed consent from all contributing women, following a protocol approved by the Danish Regional Committee on Health Research Ethics (KF-V.100.1735/90). Samples from adult human brain were obtained with approval from the Danish Regional Committee on Health Research Ethics (H-17016416).

### Histology and immunohistochemistry

Prox1-EGFP<sup>+</sup> mice and wildtype mice were anesthetized with K/X and perfused transcardially with 10 mL 0.01 M phosphate buffer saline (PBS, pH 7.4, Sigma-Aldrich, MO, USA) followed by 30 mL of 4% paraformaldehyde solution (PFA, Sigma-Aldrich) diluted in PBS and pH adjusted to 7.4. Prox1-EGFP<sup>+</sup> mice were decapitated while deeply anesthetized, and their brains fixed by overnight immersion in 4% PFA at 4 °C, for vibratome sectioning. The meninges, brain and kidneys were harvested and post-fixed in 4% PFA overnight. Brain samples were sectioned using a vibratome (50, 100 or 200 µm thick sections; Leica VT1200S, Wetzlar, Germany). After PBS washes, histological sections of the brain and meninges were blocked for one hour at room temperature (RT) in a solution containing 0.3% Triton X-100 (Sigma-Aldrich, MO, USA) and 5% normal donkey or goat serum (Gibco™; Thermo Fisher Scientific, MA, USA) in PBS followed by incubation overnight at 4 °C with primary antibodies (**Table S1**) diluted in blocking solution, then incubation with the appropriate secondary antibodies coupled to fluorophores (Alexa Fluor, 1:500; Invitrogen™ Molecular Probes™; Thermo Fisher Scientific) for two hours at RT. For VEGFR3 immunostaining, meningeal whole mounts were blocked in PBS containing 3% Bovine Serum Albumin (BSA, Sigma-Aldrich, MO, USA), 0.1% Triton X-100 and 0.05% Tween 20 (Bio-Rad) for 1h at RT, followed by overnight incubation with primary antibody diluted with PBS containing 1% BSA and 0.1% Triton X-100. For antibodies produced in mice, Fab fragment was added to the blocking solution to avoid the recognition of endogenous antibodies by the secondaries (20-40

$\mu\text{g/ml}$ , AffiniPure Fab Fragment Goat Anti-Mouse IgG (H+L), 115-007-003, Jackson ImmunoResearch, PA, USA). The next day, fluorophores coupled to secondary antibodies were incubated for 2h at RT diluted in the same antibody solution. DAPI (4',6-diamidino-2-phenylindole, Thermo Fisher Scientific, 1  $\mu\text{g/mL}$  diluted in PBS) was used for nuclear counterstaining and sections were mounted on glass slides using Prolong Gold Antifade Reagent (Invitrogen/Thermo Fisher Scientific, Carlsbad, CA, USA). Images of the immunolabeled sections and meninges were acquired with a confocal microscope (Nikon Eclipse Ti, Tokyo, Japan) using Plan Fluor 20X/0.75, 40X/1.30 and 60x/1.4 oil objectives, as previously described (47, 48). For immune-characterization of meningeal layers and immune cells, images were acquired using the Prox1-eGFP signal to ensure SLYM location, ensuring a randomization for immune cell quantification. Researchers were blind to the experimental group (young, aged or LPS-treated). Images were analyzed using FIJI/ImageJ (54). Paraffin-embedded sections of human brain and brains and kidneys from C57BL/6JRj mice were processed according to standard protocols. In brief, endogenous peroxidase activity was quenched and non-specific binding was inhibited by incubation for 30 minutes with 10% goat serum (Biological Industries, Kibbutz Beit-Haemek, Israel) at RT. Sections were incubated overnight at 4 °C with primary antibodies (extended data in **Table S1**) diluted in 10% goat serum and washed with Tris buffered saline (pH 7.4). For subsequent bright-field light microscopy analysis the REALTM EnVision™ Detection System, consisting of peroxidase/diaminobenzidine<sup>+</sup> (DAB<sup>+</sup>) rabbit/mouse (K5007, Dako, Glostrup, Denmark), was used to detect the primary antibodies. The paraffin sections were counterstained with Mayer's hematoxylin, dehydrated in graded alcohols, and cover-slipped with Pertex mounting medium (for details on bright-field microscopy, see (49)). Additionally, the entire heads and torsos from perfusion-fixed Prox1-EGFP<sup>+</sup> mice were decalcified over three weeks with 10% EDTA in Tris buffer (pH 7) at RT, prior to paraffin embedding and serial sectioning. Sections were processed for immunohistochemistry for EGFP protein detection as described above.

#### Cranial window surgery for 2-photon imaging

For all procedures involving 2-photon imaging, mice were anesthetized with K/X as previously described. Their body temperature was maintained at 37 °C using a thermostatically controlled rodent heating pad during surgery and the entire imaging session. When reflexes ceased, a 4 mm-diameter craniotomy was performed using a dental drill centered above the barrel-field cortex approximately 2.5 mm posterior to bregma. To prevent overheating, ice cold artificial cerebrospinal fluid (aCSF, 135 mM Na<sup>+</sup>, 142.8 mM Cl<sup>-</sup>, 4.2 mM K<sup>+</sup>, 1 mM Ca<sup>2+</sup>, 0.8 mM Mg<sup>2+</sup>, 10 mM glucose, 10 mM HEPES) was continuously perfused over the skull while drilling. When sufficiently thinned, the bone was gently removed with a 30G needle, and a circular 4 mm diameter coverslip was mounted in its place. The coverslip was fixed to the skull with dental cement (C&B Metabond®, Parkell, NY, USA). For *in vivo* vasculature labelling, a tail-vein injection of 500  $\mu\text{L}$ , 10 mg/ml Cascade Blue conjugated dextran (10 kDa, D1976, Invitrogen/Thermo Fisher Scientific, CA, USA) or tetramethylrhodamine dextran (200 kDa, D7139, Invitrogen/Thermo Fisher Scientific, CA, USA) was performed. For parenchymal SR101 labelling, dura mater was removed and 50  $\mu\text{M}$  of sulforhodamine 101 (SR101) diluted in sterile aCSF (S7635, Sigma-Aldrich, MO, USA) was applied topically to the brain for 15 min and then washed off with aCSF. To obtain *in vivo* images of SR101, dura, Prox1-EGFP, and vasculature in the same brain region (**Fig. 1A**), dura, vasculature and Prox1-eGFP was initially imaged (see two-photon *in vivo* imaging section) prior to the removal of dura. Following durement and SR101 application, SR101, Prox1-EGFP

and vasculature was then imaged, and the stacks were registered *post-hoc* (see image analysis and processing section).

### CSF tracer and microsphere injections in cisterna magna

For all microsphere or tracer injections, Prox1-EGFP<sup>+</sup> or wildtype mice were anesthetized with K/X and upon cessation of reflexes, a cannula consisting of a polyethylene tubing (0.024 “OD x .011” OD ID, Scandidact) was inserted into the cisterna magna (CM) for delivery of tracers diluted in aCSF as previously described (50-52). The cannula was connected to a syringe (Hamilton syringe GASTIGHT<sup>®</sup>, 1700 series, 1710TLL, volume 100  $\mu$ L, PTFE Luer lock, Reno, NV, USA) in a syringe pump (LEGATO<sup>®</sup> 130 Syringe pump, KD Scientific, Holliston, MA, USA). For all CM injections, red dextran tracer (TMR, 3 kDa, 5 mg/ml, Invitrogen/Thermo Fisher Scientific, CA, USA) or blue FluoSpheres<sup>™</sup> (carboxylate-modified, 1  $\mu$ m, 350/440 nm, F8815, Invitrogen/Thermo Fisher Scientific, CA, USA) diluted 1:10 in aCSF were injected into the CM at a controlled rate of 1  $\mu$ L/min for a total volume of 10  $\mu$ L. CSF is produced in mice at a slow rate of 80 nl/min or at a rate which is insufficient to significantly dilute the microspheres during the course of the experiments (53). The body temperature was maintained at 37 °C during all surgical procedures and imaging, using a thermostatically controlled rodent heating pad (Rodent Warmer X2 - Stoelting Co., IL, USA).

### Subdural injection of microspheres

For subdural injections of red FluoSpheres<sup>™</sup> (polystyrene, 1  $\mu$ m, 580/605 nm, F13083, Invitrogen/Thermo Fisher Scientific, CA, USA), a craniotomy was performed in Prox1-EGFP reporter mice as described above. The underlying dura mater was gently punctured at the edge of the craniotomy and lifted using fine forceps, allowing subdural insertion of a 35G needle at an 85° angle mounted to a stereotaxic arm. An estimate of 100-200  $\mu$ L of red FluoSpheres (diluted 1:50 in aCSF) were perfused under the dura mater to create an even distribution of FluoSpheres below the dura of the craniotomy. After perfusion, the needle was gently pulled out and a coverslip was mounted with dental cement. For quantitative analysis of the FluoSpheres distribution, we generated maximum projection images of the optical sections obtained above and below the EGFP<sup>+</sup> SLYM. It is important to note that while a 1:10 dilution of FluoSpheres were used for CM injections, we diluted FluoSpheres for subdural injections 1:50 to account for the additional CSF dilution/FluoSpheres entrapment which occurs when FluoroSpheres circulates from the CM to the perivascular space of dorsal arteries. These dilutions were determined empirically with the goal of achieving similar particle densities above and below SLYM.

### Rhodamine 6G injection and lipopolysaccharides (LPS) injections

Prox1-EGFP<sup>+</sup> mice received a tail vein injection of 50  $\mu$ L Rhodamine 6G (Rhod6G, 0.1%, sigma-Aldrich, MO, USA) diluted in sterile 0.9% saline (Sigma-Aldrich, MO, USA) 24 hours prior to imaging (35). Mice were imaged on the 2-photon setup. Following imaging, the mice were transcardially perfused while under deep anesthesia. The meninges and the brain were harvested and processed for immunohistochemistry.

To induce acute systemic inflammation, a subset of Prox1-EGFP<sup>+</sup> mice received an i.p. injection of LPS (4 mg/kg) 24 hours prior to imaging (54). Control mice received sterile 0.9% saline i.p. in the same volume ratio as LPS injected mice. To evaluate changes with aging, 12–13-month-old mice were used. A separate experiment was performed to assess the effect of the LPS dose on BBB integrity (**Fig. S8**).

### Blood brain barrier assay

Control and LPS-treated animals were anesthetized with Ketamine/Dexmedetomidine (K/D: 75 mg/kg, 1 mg/kg). Once the pedal reflex was lost, animals received an i.v. injection of Evans Blue (2% w/v in sterile saline, 0.2 mL/25 g of mouse) that was allowed to freely circulate for 2 hours. Then, animals were intracardially perfused with 20 mL of PBS (pH 7.4, Sigma-Aldrich, MO, USA) to eliminate the remaining intravascular Evans Blue. Brains were quickly extracted and dissected to separate left and right forebrain, and hindbrain. One half of the forebrain was drop fixed in 4% PFA overnight. 100  $\mu$ m-thick vibratome (Leica VT1200S, Wetzlar, Germany) slices of the fixed forebrain half were mounted with Prolong Gold Antifade Reagent (Invitrogen/Thermo Fisher Scientific, CA, USA) and imaged with a fluorescence stereomicroscope (Leica M205 FA) with a Hamamatsu ORCA-Flash4.0 V2 Digital CMOS camera using LAS X Leica software. The other half of forebrain was weighed, placed in 200  $\mu$ L of PBS and homogenized on ice (POLYTRON<sup>®</sup> PT 1200, Kinematica AG, Switzerland). Then, 800  $\mu$ L of formamide (11814320001, Sigma-Aldrich, MO, USA) was added to the homogenate and the mixture was incubated for 72 hours at 65°C. The resulting solution was centrifugated at 16,000g for 20 minutes to precipitate any remaining tissue. The supernatant was spectrophotometrically quantified at 620/680 nm (SpectraMax iD3, Molecular Devices, CA, USA), using a calibration curve to determine Evans Blue concentration ranging from 0.02 to 10  $\mu$ g/ $\mu$ L. Curve fit was calculated with CurveExpert (version 1.4, Hyams Development). The hindbrain was weighed ( $W_{\text{wet}}$ ), placed at 65 °C for 48 hours and the dry weight ( $W_{\text{dry}}$ ) was used to calculate brain water content following the formula: % Water Content =  $(W_{\text{wet}} - W_{\text{dry}}) / W_{\text{dry}}$ .

### Two-photon *in vivo* imaging

Animals were imaged under a two-photon microscope (Thorlabs Bergamo with a Spectra-Physics InSight<sup>®</sup> DS+<sup>™</sup> laser) using a 25 $\times$  objective (25X Nikon CFI APO LWD Objective, 380 - 1050 nm, 1.10 NA, 2.0 mm WD). Second harmonic generation (SHG) of collagen fibers was initiated at 890 - 910 nm excitation and emission collected with a 447/60 nm filter (Semrock). EGFP and Rhod6G/SR101 and fluorophore conjugated dextrans were excited using 805 - 910 nm laser wavelength at <10 mW laser power and emission was collected by 447/60 nm, 525/25 nm and/or 607/70 nm filters (Semrock), respectively. Two channels were acquired at a time and a 562 nm dichroic mirror was used to split emission light for simultaneous use of 607/70 nm filter with either the 525/25 nm or the 447/60 nm, while a 495 nm dichroic mirror was used for combining 447/60 nm and 525/25 nm filters. Images with a field of view of 533  $\times$  533  $\mu$ m acquired at a 1024  $\times$  1024 or 512  $\times$  512-pixel resolution, were acquired with 0.2-0.5  $\mu$ m step size with automated ramping laser power to compensate for loss of fluorescence in depth. 3-4 Z-stacks were acquired using all combinations of the abovementioned filter sets in pairs to capture all combinations of labelled structures for *post-hoc* alignment (see analysis section). SHG and blue labelled FluoSpheres or

dextrans were both imaged with the blue filter 447/60 nm but were separated based on excitation of 860-910 nm and 805 nm respectively.

### Bioluminescence imaging

For bioluminescence imaging, young adult WT mice, anesthetized with K/X, were used. The skull over the lambda area was thinned with a dental drill head (0.7 mm). Afterwards, the bone was covered with a thin layer of transparent glue (Super Glue Precision, Loctite, Germany). A cannula was implanted into the CM for the delivery of GeNL luciferase (30) (Gene Universal Inc., DE, USA) into the CSFs as previously described (1, 50-52). Mice were then transferred to a macroscope (AZ100, Nikon, Japan) using a 1× objective (AZ Plan Apo 1x, Nikon, Japan) and head fixed (MAG-1, Narishige, Japan). Anesthesia was maintained during the whole imaging process.

Purified GeNL (44 kDa, 1 mg/ml in aCSF) was administered by injection into the CM (1 µl/min, 10 min). 30 minutes after start of GeNL injection, the distribution over the lambda area was verified by mNeogreen fluorescence (490 nm LED, CoolLED pE-4000, FITC/Cy5 dual-band filter set F56-200, AHF Analysentechnik, Germany).

FFz (433 Da, Fluorofurimazine, Promega, WI, USA) (32) was diluted according to the manufacturer's protocol in sterile PBS of pH 7.4 and administered by retro-orbital injection (25 µl stock solution diluted in 75 µl PBS pH 7.4). Bioluminescence was recorded within 10 s after the retro-orbital injection with a cooled EMCCD camera (iXon 897 Ultra, Andor, UK) over a period of 5 minutes (1 s exposure time per frame, 512 × 512 pixel, EM Gain 17 MHz at 16-bit, Conversion Gain 3×, EM Gain Multiplier 300×, temperature -72 °C). Before FFz injection, background intensity was recorded for one minute with the same settings. After GeNL+ FFz recording, Dextran TMR or Dextran Texas Red (70 kDa, D1818 and D1830, respectively, Invitrogen, MA, USA) was injected retro orbitally, excited using a 550 nm and 580 nm LED (pE-4000, CoolLED, UK), respectively, and filtered by a DAPI/TRITC dual band filter set (F56-002, AHF Analysentechnik Germany) to obtain a map of the vasculature. Images were collected with NIS-Elements AR (Version 5.02.00, Nikon, Japan), stored as uncompressed tiff files, and post-processed with FIJI/ImageJ. For control mice, only FFz was injected retro-orbitally and recorded as described above. For bioluminescence recordings in the ear, the edge of the right ear of an anesthetized (K/X) mouse was pinned with a needle under the macroscope. 30 µl GeNL was injected into the ear tissue and the tracer distribution was verified within 10 s by its fluorescence. FFz was then administered by retro-orbital injection and bioluminescence was recorded within 10 s over a period of 5 min as described above. Background signal was recorded prior to FFz injection with the same settings for 1 min. Vasculature was stained by retro-orbital injection of Dextran TMR.

### Processing and analysis of two-photon images

3D rendering and image processing of two-photon microscope imaging was performed using IMARIS software (x64 9.7.2, Bitplane AG, Zurich, Switzerland). In case of **Fig. 1A**, a 3D minimum filter was applied using FIJI/ImageJ software to the SR101 labelled stack to emphasize the brain parenchymal outline rather than individual cells. Z-stacks obtained with different filter configurations were added as separate images and aligned using the SLYM EGFP layer or TMR dextran labeled vessels as reference. The 2-photon Z-stacks were used to calculate the thickness of dura and SLYM. To achieve this, orthogonal planes along the datasets were obtained through the “Ortho slicer” function and the “Measurement points” tool was used to measure three different

locations from both dura and SLYM for each mouse. To segregate the dura from SAS vasculature, vessels were segmented based on their location using the “Surface” function, and masks were posteriorly applied to generate different channels for each vessel type. For the quantification of microspheres, image stacks obtained with two-photon imaging were analyzed using the “Spots” function. A region of interest (ROI) with a fixed volume of  $1.2 \times 10^6 \mu\text{m}^3$  was placed above and below the SLYM layer. Elongation of the XY diameter into the Z axis was considered due to motion artifacts ( $4 \mu\text{m}$  for blue spheres,  $6 \mu\text{m}$  for red spheres). Later, spheres were automatically detected through the utilization of a quality filter. To quantify the Rhodamine 6G<sup>+</sup> cells in the dura and SLYM layer, two-photon images were analyzed using the “Surface” function, after placing a region of interest with a fixed volume of  $2.5 \times 10^6 \mu\text{m}^3$  in both dura and SLYM. Sphericity and volume filters, set to detect Rhod6G<sup>+</sup> volumes above  $40 \mu\text{m}^3$ , were applied to disregard the interference of nonspecific labelling in the final numbers. Similarly, to analyze SLYM permeability, three ROIs with a fixed volume of  $4 \times 10^3 \mu\text{m}^3$  were placed both below and above the membrane. The “surfaces” created inside these ROIs were used to measure the mean signal intensity of the tracer injected. Two-tailed unpaired t-tests with Welch’s correction were performed to analyze both Rhod6G and SLYM permeability assays. A two-tailed unpaired t-test was used to analyze microsphere experiments. All statistical analyses were performed using GraphPad Prism 9.3.1 software for macOS (GraphPad Software, CA, USA).

#### Processing and analysis of bioluminescence images

Line profiles of the bioluminescence intensity distribution from the venous sinus lumen into the subarachnoid space were calculated in FIJI/ImageJ (55). First, the average intensity of the background recording before FFz injection was subtracted from the average of the bioluminescence recording across the field of view. Second, ROIs perpendicular to the vascular wall were selected in the inverted GeNL fluorescence channel (shadow imaging) or vascular tracer channel. The intensity profiles of the ROIs from the GeNL + FFz recording (Bioluminescence Light Intensity, BLI) and from the shadow imaging or vascular tracer channel (Fluorescence Light Intensity, FLI) were normalized to their minima and maxima, respectively, and plotted together centered around their intersection. A clear vessel border was not always visible due to the thickness of the superior sagittal sinus and the low resolution in Z from the macroscopic recordings. Therefore, the intersection of the profiles was used as a center point to compare several line profiles from multiple recordings and mice.

For the bioluminescence study in the ear, raw images were post-processed as described above. ROIs were manually drawn within and outside the enzyme and substrate intensity areas and the normalized fluorescence and bioluminescence intensity, respectively, were plotted. The average pixel intensity per ROI was normalized to the average mean pixel intensity derived from the within injection areas. For analysis, a two-tailed unpaired t-test was performed.

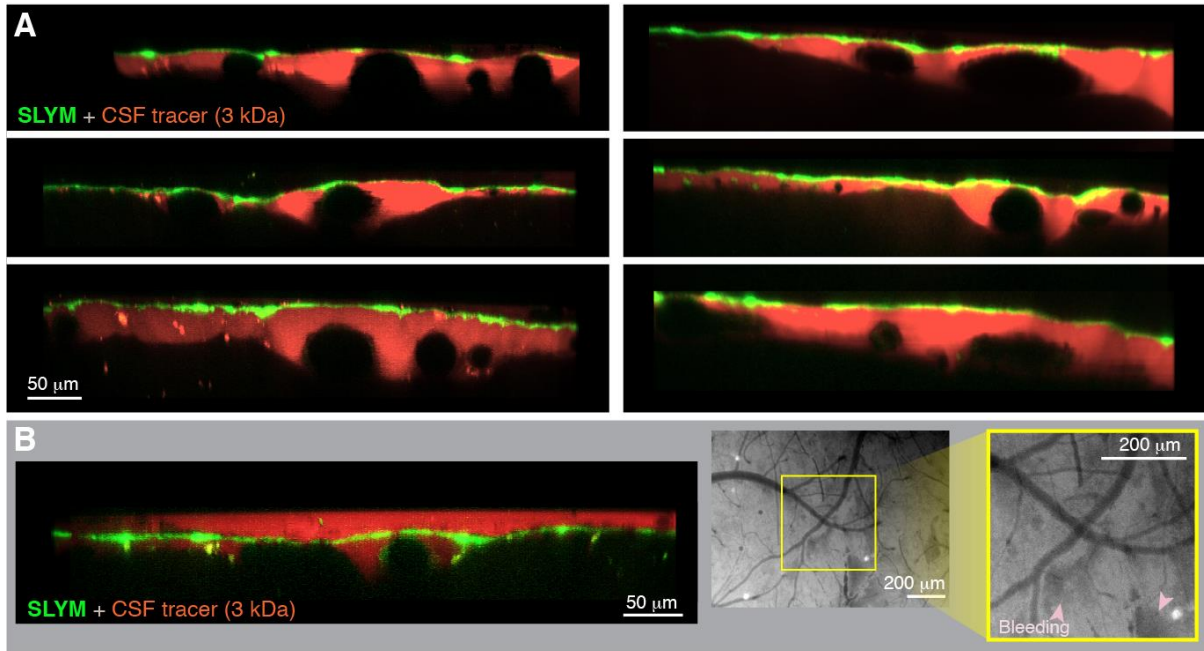


**Fig. S1. SLYM acts as a barrier for a 3 kDa CSF tracer.** A cranial window (4 mm) was prepared over the sensorimotor cortex in ketamine/xylazine anesthetized Prox1-EGFP mice. A 3 kDa tracer (TMR-dextran, red) was injected into cisterna magna and allowed to circulate for 30 - 60 min before imaging. **(A)** Orthogonal sections of 2-photon z-stacks (0.2-0.5  $\mu\text{m}$  step-size) show that SLYM (green) represents a barrier that restricts dispersion of the 3 kDa CSF tracer. The red CSF tracer is confined to the lower deep subarachnoid space and does not enter the upper superficial subarachnoid compartment. The panel display orthogonal sections obtained by 2-photon imaging of 6 Prox1-EGFP mice. Scale bar: 50  $\mu\text{m}$ . **(B)** In a subset of experiments, surgical damage caused tears in dura and SLYM resulting in loss of the barrier properties of SLYM. An orthogonal section representative of preparations with noticeable bleedings in dura shows that the 3 kDa tracer (red) is present at both sides of SLYM. Bright-field images of a cranial window preparation highlight the bleeding in the dura from the same Prox1-EGFP mouse (pink arrowheads). Yellow square indicates the field of view imaged in the 2-photon z-stacks. Scale bars, 2-photon image: 50  $\mu\text{m}$ ; bright-field images: 200  $\mu\text{m}$ . *CSF*: Cerebrospinal fluid; *SLYM*: Subarachnoid Lymphatic-like Membrane.

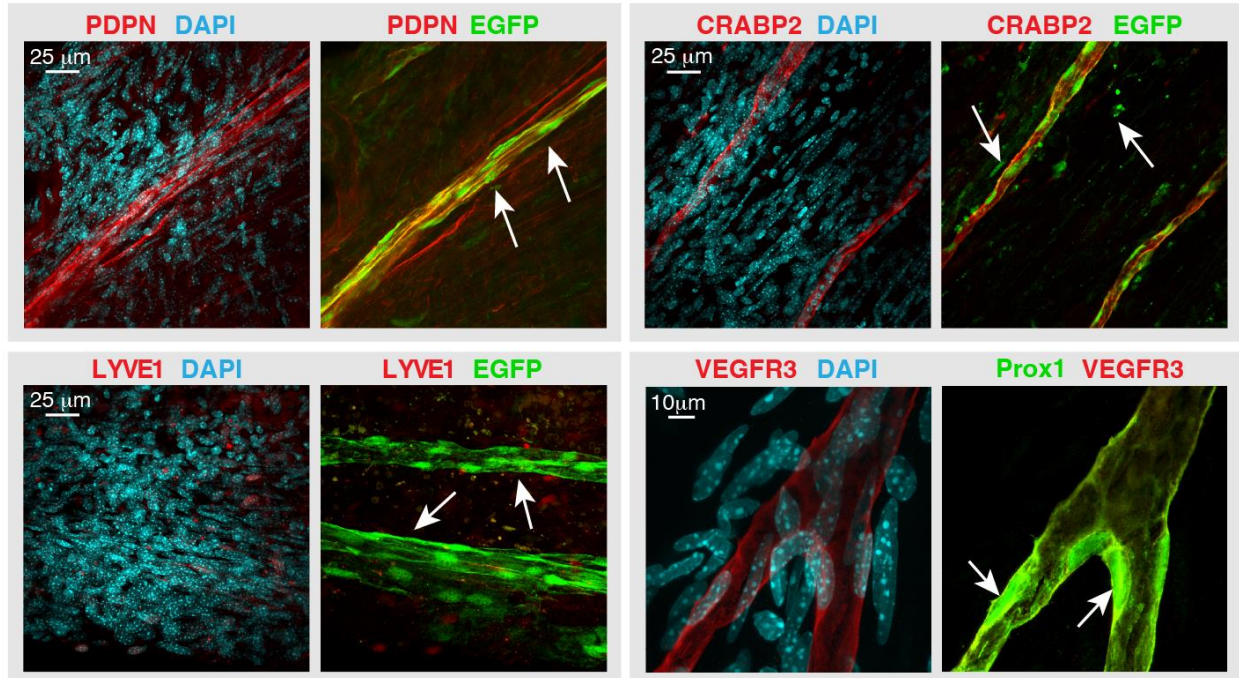


**Fig. S2. Immune-phenotypic characterization of dural lymphatic vessels in dura mater whole mount ex vivo preparations.** Dural preparations only contain patches of SLYM in blood vessel areas, where SLYM is in close contact with the sinuses. Immunolabelling of meninges from Prox1-EGFP<sup>+</sup> mouse for PDPN, CRABP2, LYVE1, and VEGFR3 (all in red) show that LYVE1 and VEGFR3 immunoreactivities are restricted to endothelial cells of lymphatic vessels (arrows). *PDPN: Podoplanin.*

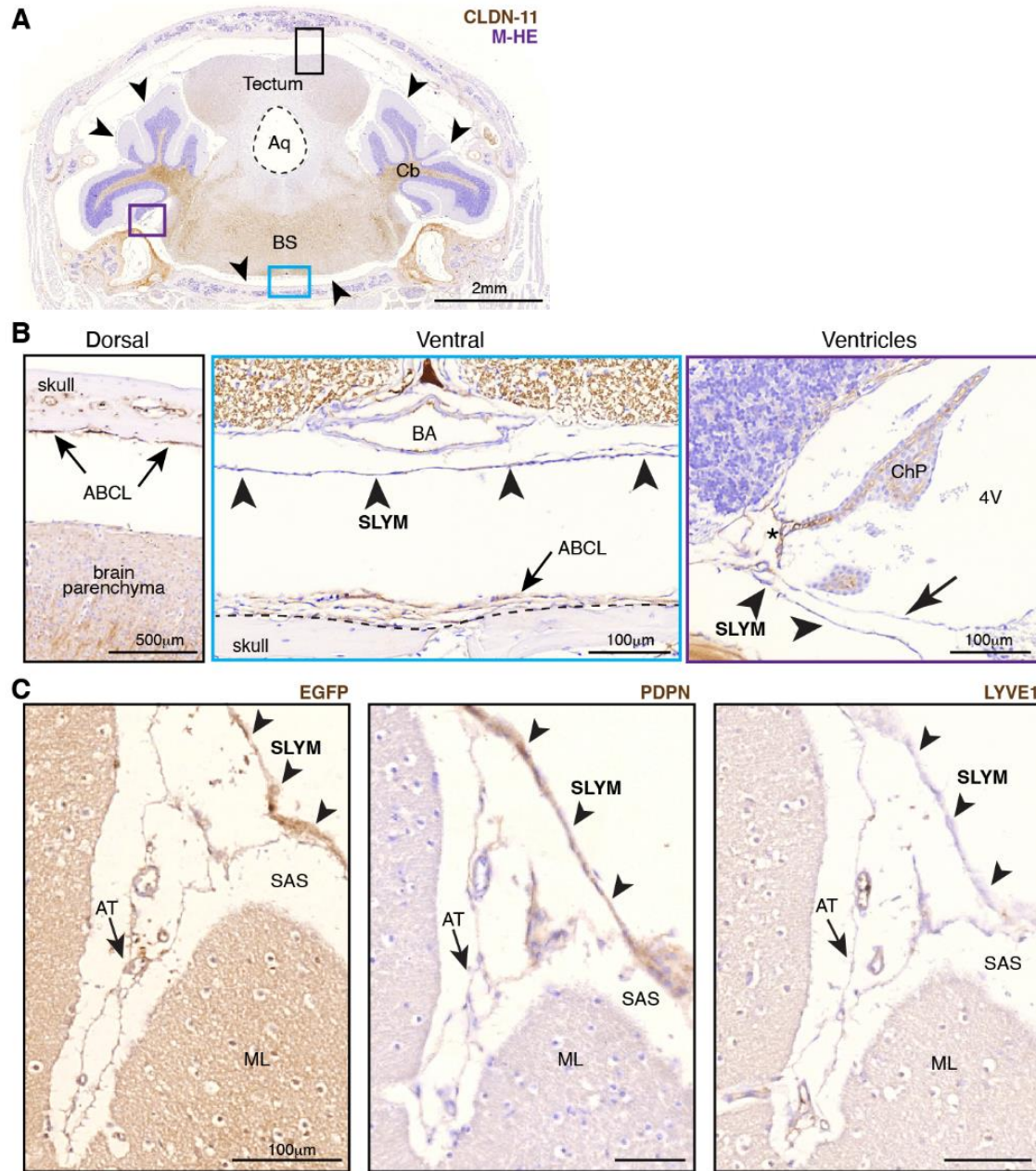


**Fig. S3. SLYM does not correspond to the arachnoid mater structures. (A-B)** Decalcified whole head sections of Prox1-EGFP<sup>+</sup> mouse counterstained with Mayer's hematoxylin (M-HE, purple) and immunolabeled for CLDN-11 show the arachnoid barrier cells adjacent to the skull in the dorsal and ventral regions (arrows), and stromal cells of the choroid plexus (asterisk). Neither SLYM (arrowheads) nor tela choroidea cells (sharp-edged arrow) are CLDN-11<sup>+</sup>. **(C)** In the inner subarachnoid space between the cerebellar folia arachnoid trabeculae (EGFP<sup>+</sup>/ PDPN<sup>-</sup>/ LYVE1<sup>-</sup>, arrows) are present. *ABCL*: arachnoid barrier cell layer; *AT*: arachnoid trabeculae; *Cb*: cerebellum; *ChP*: choroid plexus; *ML*: molecular layer; *SAS*: inner subarachnoid space; *SLYM*: Subarachnoid Lymphatic-like Membrane.

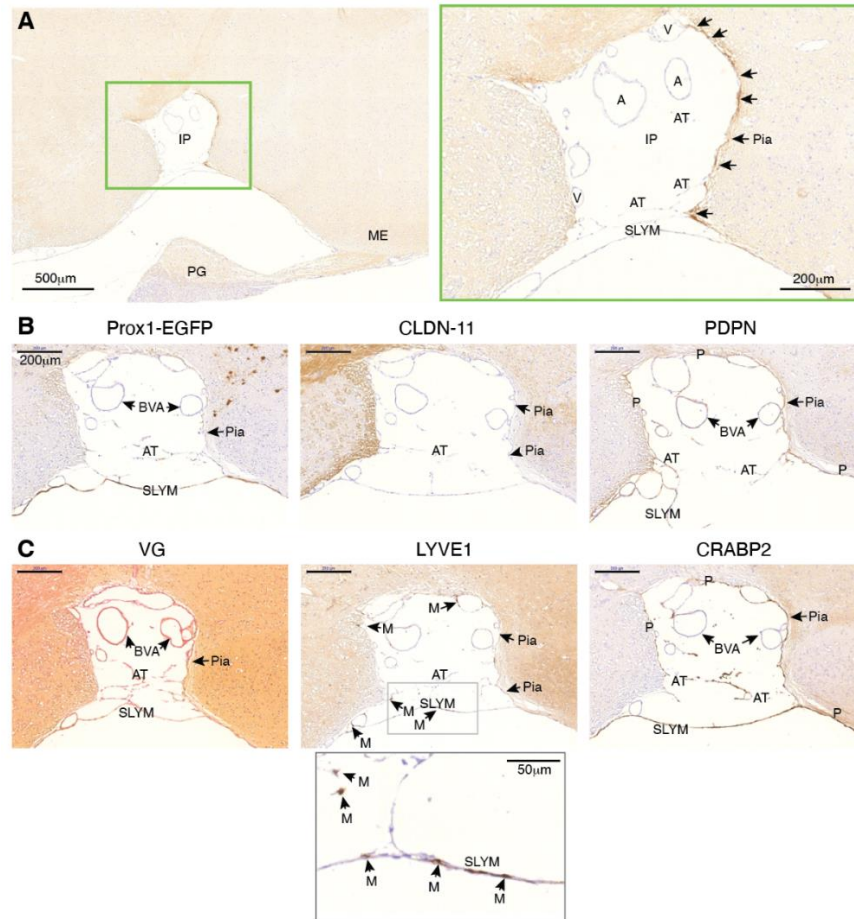


**Fig. S4. Immunophenotypic characterization of meningeal membranes and the arachnoid trabeculae.** (A) Midsagittal section through the median eminence (ME) and pituitary gland (PG) showing pia in the rostral part of the interpeduncular cistern (IP) positively stained for VEGFR3 depicted on the right in higher magnification (green box) and indicated by arrows. Arteries (A), veins (V), cross-sectioned arachnoid trabeculations (AT) and SLYM show no immunoreactivity. (B) Consecutive sections from the same mouse stained for Prox1-EGFP, Claudin-11 (CLDN) and Podoplanin (PDPN). Only SLYM is positively stained for Prox1-EGFP in contrast to the negative pia, arachnoid trabeculations, and blood vessel adventitia (BVA). CLDN-11 shows no reactivity, whereas the entire pia (arrows), arachnoid trabeculations, blood vessel adventitia and SLYM show positive PDPN-reactivity. (C) Consecutive sections depicting van Gieson-stained collagen (VG, red) in adventitia of blood vessels (BV), arachnoid trabeculations (AT), pia and SLYM, followed by staining for LYVE1. Only macrophages (M) associated with SLYM, pia, arachnoid trabeculations, and blood vessels are immunoreactive for LYVE1. Insert shows in higher magnification LYVE1<sup>+</sup> macrophages associated with SLYM. Staining for CRABP2 shows that all relevant meningeal components in the inner SAS are strongly reactive for CRABP2. All images in B and C are of the same magnification. See scale bar in B. A: artery; AT: arachnoid trabeculations; BV: blood vessel; BVA: blood vessel adventitia; CLDN: Claudin-11; IP: interpeduncular cistern; M: macrophages; ME: median eminence; PDPN: Podoplanin; PG: pituitary gland; SLYM: Subarachnoid Lymphatic-like Membrane; v: vein; VG: van Gieson-stained collagen.

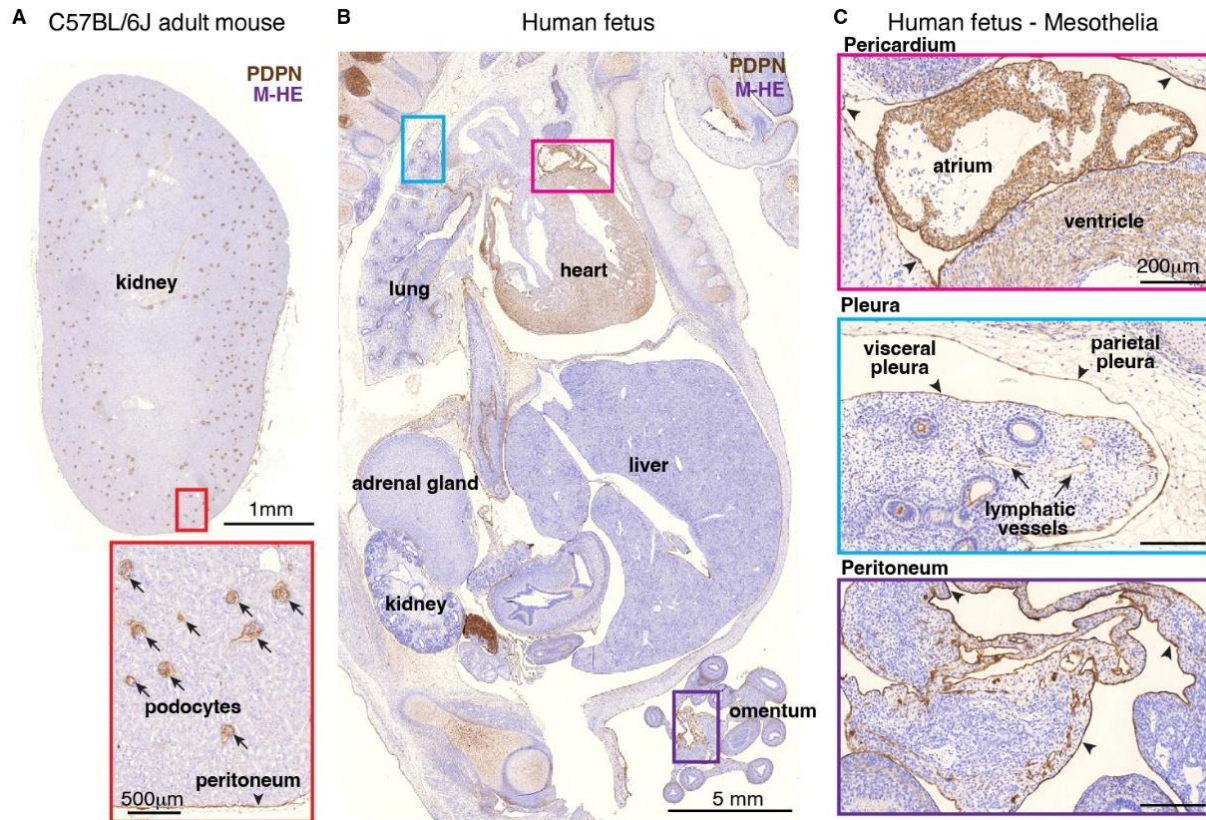


**Fig. S5. PDPN<sup>+</sup> mesothelia in mouse and human peripheral organs and cavities.** (A) Paraffin-embedded section obtained from adult C57BL/6J mice kidneys was processed for immunohistochemistry and counterstained with Mayer's hematoxylin (M-HE, purple). PDPN<sup>+</sup> podocytes (arrows) are detected, as well as the PDPN<sup>+</sup> peritoneum (arrowhead). (B) Histological section from human fetus showing the thoracic and abdominal cavities. (C) PDPN<sup>+</sup> mesothelial membranes (arrowheads) corresponding to the pericardium in the heart, pleura in the lungs, and peritoneum in the mesentery. PDPN<sup>+</sup> lymphatic vessels are also observed in the lungs (arrows) and in the mesentery. *M-HE*: Mayer's hematoxylin; *PDPN*: Podoplanin.

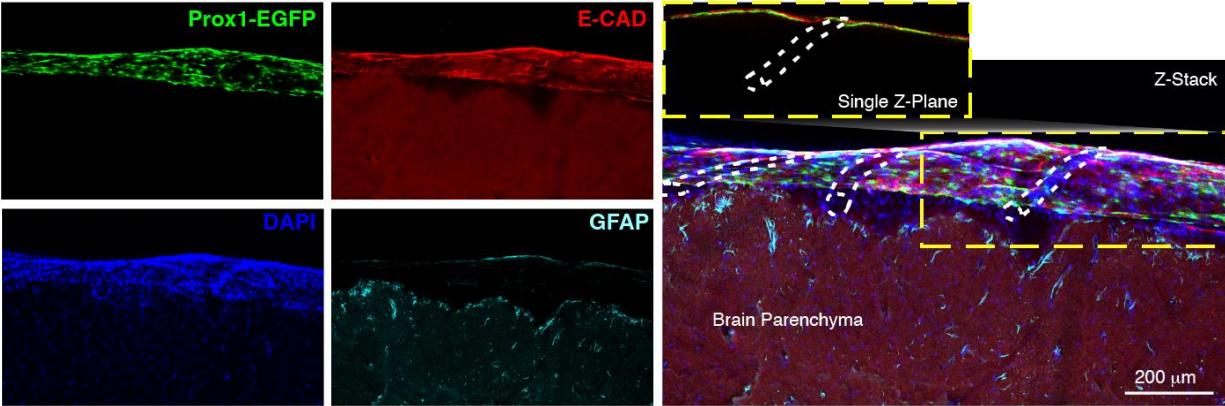


**Fig S6. The arachnoid barrier cell layer markers E-Cadherin and Prox1-EGFP do not colocalize.** Z-Stack maximum projections of confocal images of immunohistochemistry showing the brain surface covered by SLYM (Prox1-EGFP, green) and arachnoid (ABC layer marker E-Cadherin, red) in non-overlapping pattern. Astrocytes and nuclei are labelled by GFAP (cyan) and DAPI (blue) for clarity. A single plane image is shown to depict the absence of colocalization. *E-CAD: E-Cadherin, GFAP: Glial Fibrillar Acidic Protein.*

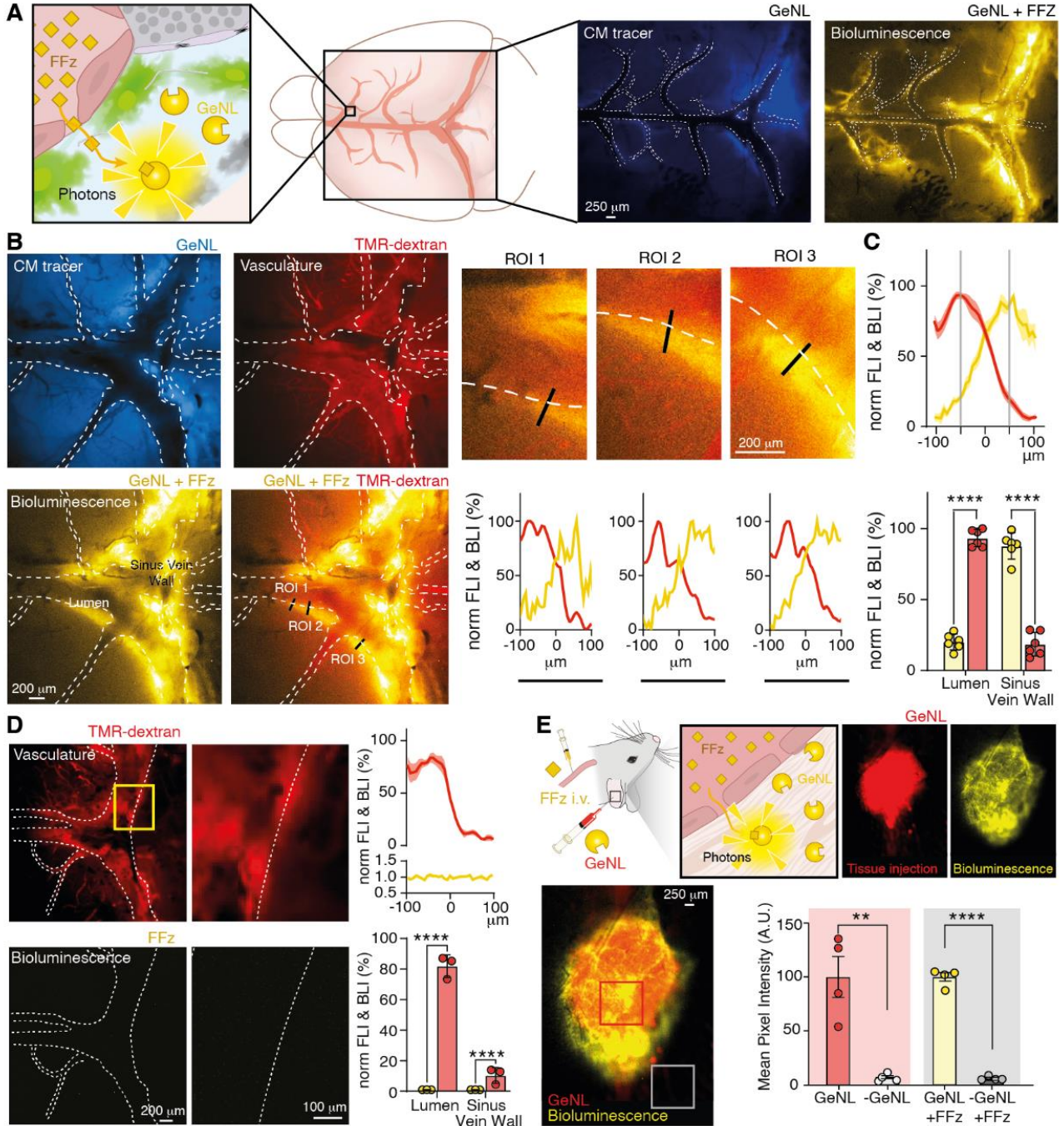


**Fig. S7. Direct exchange of a small solute across the wall of the dural venous sinus and CSF.**

(A) Scheme of the arrangement of SLYM directly contacting the venous endothelial cells. *In vivo* bioluminescence assay to access direct transport of molecules from the venous blood to the CSF: Luciferase (GeNL) was injected into the CSF in cisterna magna and its substrate (FFz, 433 Da) delivered *i.v.*. The inverted Luciferase signal was used to outline the vascular compartment indicated by a dashed white line. A bioluminescence signal (photons) is generated when the substrate, FFz binds to luciferase (GeNL). (B) Left panel: GeNL fluorescence, TMR-Dextran fluorescence, bioluminescence signal after substrate injection, and overlay of the bioluminescence

signal and the vasculature at the sinus veins. The dextran labeled vasculature is outlined by a white dashed line. Right panel: Line plots of three representative regions of interest (ROIs, black lines) placed perpendicular to the sinus vein crossing the vein wall, centered around their intersection ('zero' distance) and normalized to their minima and maxima values, respectively. (C) Top panel: Average intensity distribution of the bioluminescence signal (yellow) generated by the luciferase reaction, and inverted mNeogreen intensity as shadow mapping for vasculature (red) after normalization to their minima and maxima values. Signal intensities are plotted as a function of the distance from their intersection to display photon generation perpendicular to the sinus vein wall (mean  $\pm$  SEM, n = 8, avg of 3 – 4 ROIs per mouse). Lower panel: Bar plot representation of the fluorescence intensity  $\pm$  50  $\mu$ m from the intensity intersection. (Two-tailed unpaired t-test,  $p < 0.0001$ , n=8). (D) Control experiments with i.v. delivery of FFz only. No bioluminescence signal was generated. Top panel: Fluorescence intensity of the i.v. tracer (red) at the vessel wall normalized to their minima and maxima values. Bioluminescence intensity of FFz (yellow) normalized to the average signal over the whole line plot. Lower panel: Bar plot representation of the fluorescence and bioluminescence intensity  $\pm$  50  $\mu$ m from the 50 % intensity of the normalized i.v. tracer signal. (two-sample two-tailed unpaired t-test,  $p < 0.0001$ , n = 3). Scale bar 200  $\mu$ m, insert scale bar 100  $\mu$ m. (E) Top Panel: *In vivo* bioluminescence assay to access direct transport of molecules from the venous blood to tissue in the ear: GeNL was injected locally into the ear tissue and FFz i.v.. Bottom Panel: Overlay of the bioluminescence signal and GeNL fluorescence at the injection site. Example ROIs for quantification of bioluminescence intensity and substrate fluorescence intensity, respectively, within and outside of the injection area are shown in red (within) and white (outside). Bar plot of the normalized pixel intensities within and outside of the injection area (Two-tailed unpaired t-test,  $p < 0.0001$ , n = 4). Significance shown as: \* $p < 0.05$ , \*\* $p < 0.01$ , \*\*\* $p < 0.001$ , \*\*\*\* $p < 0.0001$ . A. U.: arbitrary units; BLI: Bioluminescence Light Intensity, CM: Cisterna Magna, FFz: Fluorofurimazine; FLI: Fluorescence Light Intensity; GeNL: GeNL luciferase; i.v.: intravenous; norm: normalized; ROI: Region of Interest, TMR: Tetramethylrhodamine.

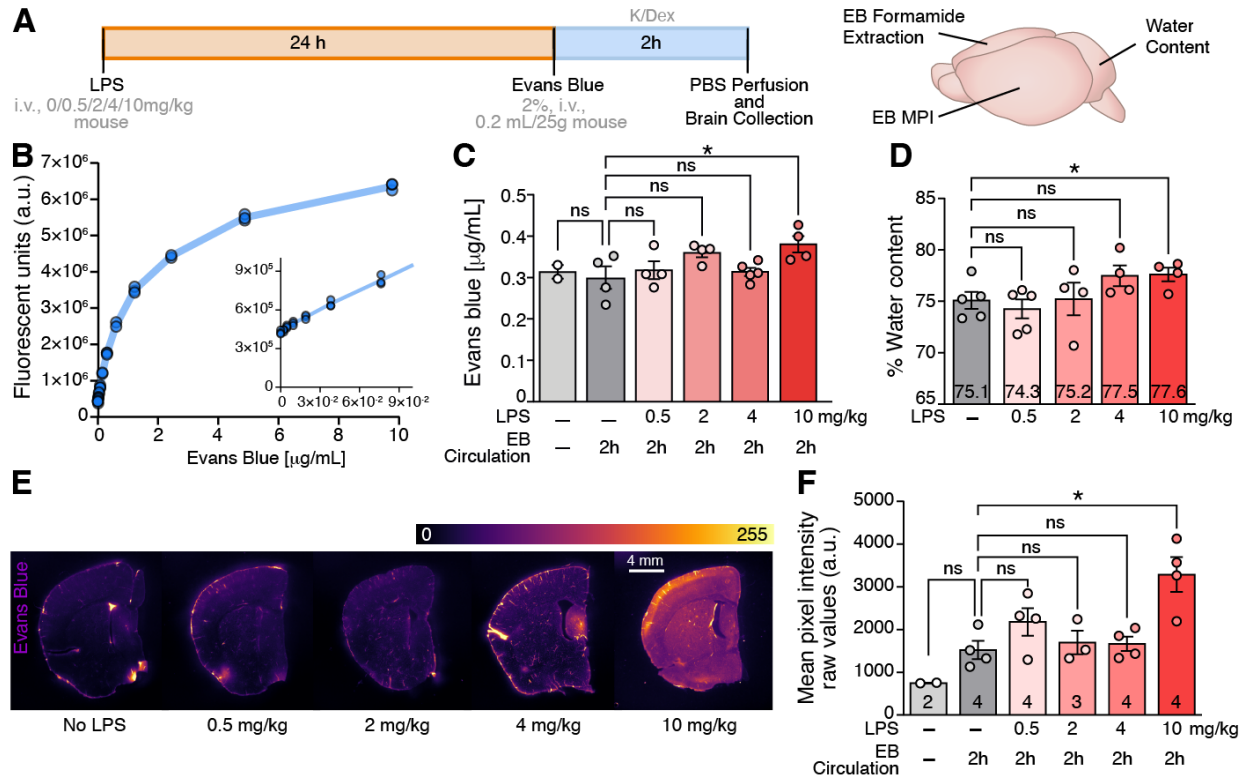


**Fig. S8: Blood-Brain Barrier opening in response to LPS treatment.** (A) Scheme of the performed experiments. Animals were treated with different doses of LPS 24 hours before the permeability assay. (B) Graph showing a representative calibration curve depicting the fluorescent signal increase in relation to Evans Blue concentration. Line represents mean of three replicates, that are individually shown as dots. One-way ANOVA,  $p = 0.04$ . (C) Bar graph showing the mean  $\pm$  SEM. Evans Blue concentration in brain determined by formamide extraction. Dots indicate animal replicates. (D) Graph of brain water content 24 hours post-LPS treatment. Bars indicate mean  $\pm$  SEM, with animals shown as dots. Kruskal-Wallis,  $p = 0.03$ . (E) Representative images showing Evans Blue presence in the brain at 620 nm channel. (F) Quantification of MPI values of fluorescence images for the six experimental groups. Bars show mean  $\pm$  SEM, while each dot is the average of 6 slices per animal. One-way ANOVA,  $p = 0.001$ . Of note, the same animals were used for formamide extraction, water content determination and MPI analysis. n is indicated in panel F for each group.

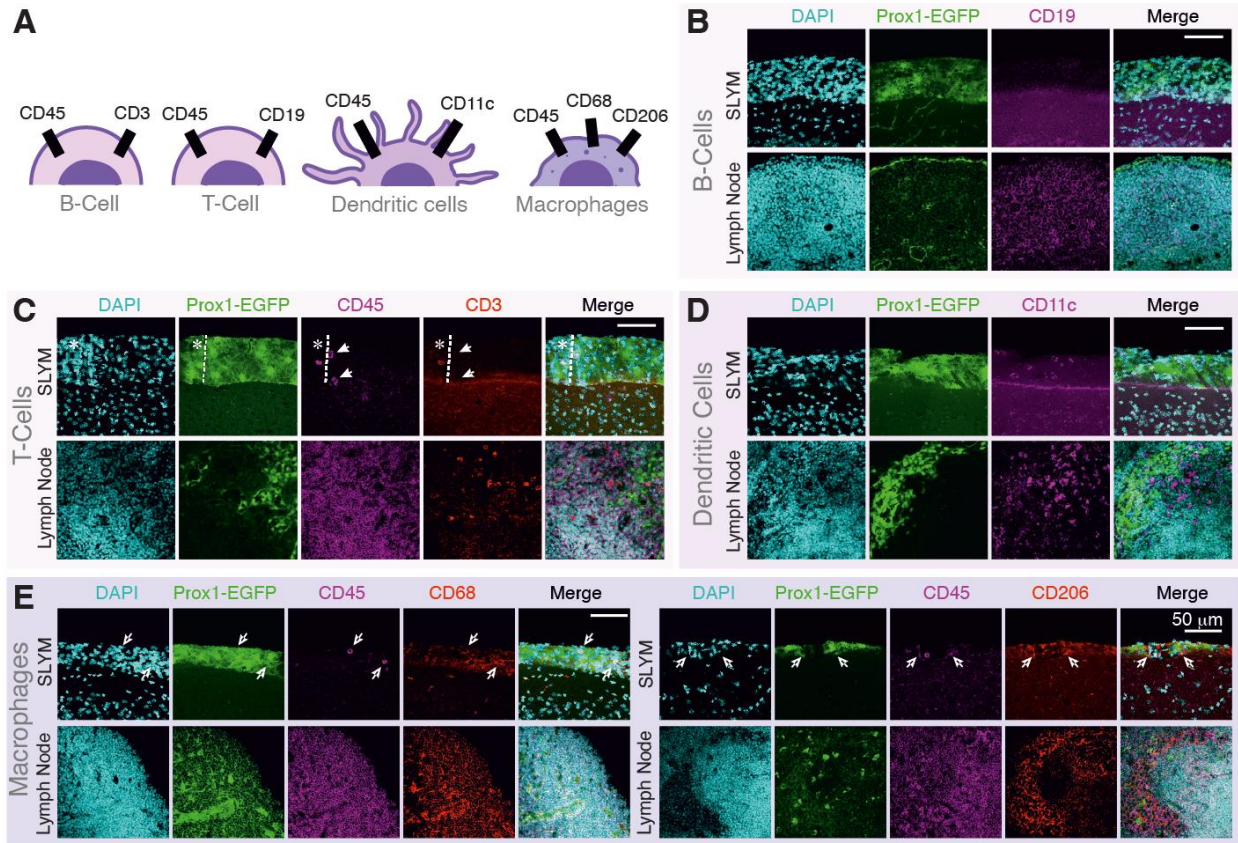


**Fig. S9: Immunophenotypical characterization of immune cells in SLYM.** (A) List of markers used for the immune characterization. (B) Confocal images of CD19 labelling showing that B lymphocytes are absent from SLYM tissue. (C) Representative confocal imaging showing that the CD45 cells found in SLYM were negative for T-cell marker (CD3<sup>+</sup>). (D) Dendritic cells identified by CD11c were found in SLYM. (E) Both CD68 and CD206 markers identified a rich macrophage population located in SLYM. Lymph node tissue from the same animals was used to validate antibody recognition of the intended antigens in all cases. *SLYM*: *Subarachnoid Lymphatic-like Membrane*.

Antigen	Immunogen	Manufacturer (CAT#)	Host & isotype	Dilution	Reference RRID#
<b>B-Lymphocytes (CD19)</b>	Recombinant fragment within Human CD19 aa 300 to the C-terminus. The exact sequence is proprietary	Abcam (ab134114)	Rabbit IgG	1:1000	AB_2801636
<b>Caveolin-1 (Cav1)</b>	Synthetic peptide corresponding to Mouse Caveolin-1 aa 1-100 (N terminal) conjugated to keyhole limpet haemocyanin	Abcam (ab18199)	Rabbit IgG	1:100	AB_444314
<b>CD11c (Integrin, alpha X - ITGAX)</b>	Mouse spleen dendritic cells	Thermo Fischer Scientific (14-0114-82)	Armenian hamster IgG	1:200	AB_467115
<b>CD206 (Mannose receptor C type 1)</b>	Chimeric CRD4-7-Fc protein	Bio-Rad (MCA2235)	Rat IgG	1:400	AB_324622
<b>CD45 (Lymphocyte common antigen)</b>	Mouse Abelson leukaemia virus-induced pre-B tumour cells	BD Pharmingen (550286)	Rat IgG2a, κ	1:100	AB_393581
<b>CD45 (Lymphocyte common antigen)</b>	Mouse myeloma cell line NS0-derived recombinant mouse CD45 Gln24-Lys425 Accession # NP_035340	R&D Systems (AF 114)	Goat IgG	1:100	AB_442146
<b>CD68 (Class D scavenger receptor)</b>	Tissue, cells or virus corresponding to Rat CD68. Rat spleen cell	Abcam (ab31630)	Mouse IgG1	1:500	AB_1141557
<b>Claudin-11 (CLDN-11)</b>	Synthetic peptide corresponding to human oligodendrocyte specific protein (C terminal)	Abcam (ab53041)	Rabbit IgG	1:800	AB_2276205
<b>E-Cadherin (E-Cad)</b>	Recombinant full-length protein	Abcam (ab231303)	Mouse IgG	1:100	AB_2923285
<b>Green fluorescence protein (GFP)</b>	Full length recombinant GFP	Aves Lab (GFP-1020)	Chicken IgY	1:1000	AB_2307313
	GFP isolated directly from <i>Aequorea victoria</i>	Thermo Fischer Scientific (A-6455)	Rabbit IgG	1:200	AB_221570

<b>Lymphatic Vessel Endothelial Receptor 1 (LYVE1)</b>	Recombinant fragment (His-tag) corresponding to murine LYVE1 aa 24-228 (C terminal)	Abcam (ab14917)	Rabbit IgG	1:100	AB_301509
<b>Podoplanin (Pdpn)</b>	Murine thymic stromal cell lines	Thermo Fischer Scientific (14-5381-85)	Syrian hamster IgG	1:400	AB_1210507
<b>Podoplanin (Pdpn)</b>	Dysgerminoma tissue	Agilent Dako (IR072)	Mouse IgG1 $\kappa$	1:75	AB_2162081
<b>T-Lymphocytes (CD3)</b>	$\gamma\delta$ TCR-positive T-T hybridoma D1	Invitrogen (14-0032-82)	Rat IgG2b, kappa	1:200	AB_467053
<b>Vascular endothelial growth factor receptor 3 (VEGFR3)</b>	Synthetic peptide within Human VEGF Receptor 3 aa 1250-1350	Abcam (ab27278)	Rabbit IgG	1:100	AB_470949
<b>Vascular endothelial growth factor receptor 3 (VEGFR3)</b>	<i>S. frugiperda</i> insect ovarian cell line Sf21-derived recombinant mouse VEGFR3/Flt-4 Tyr25-Asp770	R&D Systems (AF 743)	Goat IgG	1:100	AB_355563

**Table S1. List of primary antibodies.** Specifications of the primary antibodies.

**Movie S1.**

Video shows that FFz enters the CSF compartment at the sinus at the interface of the venous endothelium and SLYM. Composite image of bright field + TMR-dextran signal to outline the confluency of the superior sagittal sinus and transverse sinus. Left panel: FFz was injected i.v. 30 min after GeNL injection into the CSF in cisterna magna. Right panel: FFz injection i.v. only. Dotted line indicates the vascular wall outlined by intravascular TMR-dextran. Original frame rate 1 Hz.

## References and Notes

1. J. J. Iliff, M. Wang, Y. Liao, B. A. Plogg, W. Peng, G. A. Gundersen, H. Benveniste, G. E. Vates, R. Deane, S. A. Goldman, E. A. Nagelhus, M. Nedergaard, A paravascular pathway facilitates CSF flow through the brain parenchyma and the clearance of interstitial solutes, including amyloid  $\beta$ . *Sci. Transl. Med.* **4**, 147ra111 (2012). [doi:10.1126/scitranslmed.3003748](https://doi.org/10.1126/scitranslmed.3003748) [Medline](#)
2. H. Mestre, J. Tithof, T. Du, W. Song, W. Peng, A. M. Sweeney, G. Olveda, J. H. Thomas, M. Nedergaard, D. H. Kelley, Flow of cerebrospinal fluid is driven by arterial pulsations and is reduced in hypertension. *Nat. Commun.* **9**, 4878 (2018). [doi:10.1038/s41467-018-07318-3](https://doi.org/10.1038/s41467-018-07318-3) [Medline](#)
3. N. E. Fultz, G. Bonmassar, K. Setsompop, R. A. Stickgold, B. R. Rosen, J. R. Polimeni, L. D. Lewis, Coupled electrophysiological, hemodynamic, and cerebrospinal fluid oscillations in human sleep. *Science* **366**, 628–631 (2019). [doi:10.1126/science.aax5440](https://doi.org/10.1126/science.aax5440) [Medline](#)
4. H. Mestre, L. M. Hablitz, A. L. R. Xavier, W. Feng, W. Zou, T. Pu, H. Monai, G. Murlidharan, R. M. Castellanos Rivera, M. J. Simon, M. M. Pike, V. Plá, T. Du, B. T. Kress, X. Wang, B. A. Plog, A. S. Thrane, I. Lundgaard, Y. Abe, M. Yasui, J. H. Thomas, M. Xiao, H. Hirase, A. Asokan, J. J. Iliff, M. Nedergaard, Aquaporin-4-dependent glymphatic solute transport in the rodent brain. *eLife* **7**, e40070 (2018). [doi:10.7554/eLife.40070](https://doi.org/10.7554/eLife.40070) [Medline](#)
5. A. Louveau, I. Smirnov, T. J. Keyes, J. D. Eccles, S. J. Rouhani, J. D. Peske, N. C. Derecki, D. Castle, J. W. Mandell, K. S. Lee, T. H. Harris, J. Kipnis, Structural and functional features of central nervous system lymphatic vessels. *Nature* **523**, 337–341 (2015). [doi:10.1038/nature14432](https://doi.org/10.1038/nature14432) [Medline](#)
6. A. Aspelund, S. Antila, S. T. Proulx, T. V. Karlsen, S. Karaman, M. Detmar, H. Wiig, K. Alitalo, A dural lymphatic vascular system that drains brain interstitial fluid and macromolecules. *J. Exp. Med.* **212**, 991–999 (2015). [doi:10.1084/jem.20142290](https://doi.org/10.1084/jem.20142290) [Medline](#)
7. L. H. Weed, Meninges and cerebrospinal fluid. *J. Anat.* **72**, 181–215 (1938). [Medline](#)
8. A. Key, G. Retzius, *Studien in der Anatomie des Nervensystems und des Bindegewebes* (Samson & Wallin, 1876).
9. W. E. le Gros Clark, On the Pacchionian bodies. *J. Anat.* **55**, 40–48 (1920). [Medline](#)
10. K. Ohta, T. Inokuchi, Y. Hayashida, T. Mizukami, T. Yoshida, T. Kawahara, Regional diminution of von Willebrand factor expression on the endothelial covering arachnoid granulations of human, monkey and dog brain. *Kurume Med. J.* **49**, 177–183 (2002). [doi:10.2739/kurumemedj.49.177](https://doi.org/10.2739/kurumemedj.49.177) [Medline](#)
11. M. K. Rasmussen, H. Mestre, M. Nedergaard, Fluid transport in the brain. *Physiol. Rev.* **102**, 1025–1151 (2022). [doi:10.1152/physrev.00031.2020](https://doi.org/10.1152/physrev.00031.2020) [Medline](#)
12. A. Drieu, S. Du, S. E. Storck, J. Rustenhoven, Z. Papadopoulos, T. Dykstra, F. Zhong, K. Kim, S. Blackburn, T. Mamuladze, O. Harari, C. M. Karch, R. J. Bateman, R. Perrin, M. Farlow, J. Chhatwal, S. Hu, G. J. Randolph, I. Smirnov, J. Kipnis; Dominantly Inherited Alzheimer Network, Parenchymal border macrophages regulate the flow dynamics of the

- cerebrospinal fluid. *Nature* **611**, 585–593 (2022). [doi:10.1038/s41586-022-05397-3](https://doi.org/10.1038/s41586-022-05397-3) [Medline](#)
13. I. Choi, H. K. Chung, S. Ramu, H. N. Lee, K. E. Kim, S. Lee, J. Yoo, D. Choi, Y. S. Lee, B. Aguilar, Y.-K. Hong, Visualization of lymphatic vessels by *Prox1*-promoter directed GFP reporter in a bacterial artificial chromosome-based transgenic mouse. *Blood* **117**, 362–365 (2011). [doi:10.1182/blood-2010-07-298562](https://doi.org/10.1182/blood-2010-07-298562) [Medline](#)
  14. J. T. Wigle, N. Harvey, M. Detmar, I. Lagutina, G. Grosveld, M. D. Gunn, D. G. Jackson, G. Oliver, An essential role for *Prox1* in the induction of the lymphatic endothelial cell phenotype. *EMBO J.* **21**, 1505–1513 (2002). [doi:10.1093/emboj/21.7.1505](https://doi.org/10.1093/emboj/21.7.1505) [Medline](#)
  15. K. Masamoto, Y. Tomita, H. Toriumi, I. Aoki, M. Unekawa, H. Takuwa, Y. Itoh, N. Suzuki, I. Kanno, Repeated longitudinal in vivo imaging of neuro-glio-vascular unit at the peripheral boundary of ischemia in mouse cerebral cortex. *Neuroscience* **212**, 190–200 (2012). [doi:10.1016/j.neuroscience.2012.03.034](https://doi.org/10.1016/j.neuroscience.2012.03.034) [Medline](#)
  16. A. Nimmerjahn, F. Kirchhoff, J. N. Kerr, F. Helmchen, Sulforhodamine 101 as a specific marker of astroglia in the neocortex in vivo. *Nat. Methods* **1**, 31–37 (2004). [doi:10.1038/nmeth706](https://doi.org/10.1038/nmeth706) [Medline](#)
  17. K. Kothur, L. Wienholt, F. Brilot, R. C. Dale, CSF cytokines/chemokines as biomarkers in neuroinflammatory CNS disorders: A systematic review. *Cytokine* **77**, 227–237 (2016). [doi:10.1016/j.cyto.2015.10.001](https://doi.org/10.1016/j.cyto.2015.10.001) [Medline](#)
  18. H. Mestre, Y. Mori, M. Nedergaard, The brain’s glymphatic system: current controversies. *Trends Neurosci.* **43**, 458–466 (2020). [doi:10.1016/j.tins.2020.04.003](https://doi.org/10.1016/j.tins.2020.04.003) [Medline](#)
  19. M. Tomooka, C. Kaji, H. Kojima, Y. Sawa, Distribution of podoplanin-expressing cells in the mouse nervous systems. *Acta Histochem. Cytochem.* **46**, 171–177 (2013). [doi:10.1267/ahc.13035](https://doi.org/10.1267/ahc.13035) [Medline](#)
  20. S. Banerji, J. Ni, S.-X. Wang, S. Clasper, J. Su, R. Tammi, M. Jones, D. G. Jackson, LYVE-1, a new homologue of the CD44 glycoprotein, is a lymph-specific receptor for hyaluronan. *J. Cell Biol.* **144**, 789–801 (1999). [doi:10.1083/jcb.144.4.789](https://doi.org/10.1083/jcb.144.4.789) [Medline](#)
  21. M. A. Asson-Batres, O. Ahmad, W. B. Smith, Expression of the cellular retinoic acid binding proteins, type II and type I, in mature rat olfactory epithelium. *Cell Tissue Res.* **312**, 9–19 (2003). [doi:10.1007/s00441-003-0709-1](https://doi.org/10.1007/s00441-003-0709-1) [Medline](#)
  22. C. B. Brøchner, C. B. Holst, K. Møllgård, Outer brain barriers in rat and human development. *Front. Neurosci.* **9**, 75 (2015). [doi:10.3389/fnins.2015.00075](https://doi.org/10.3389/fnins.2015.00075) [Medline](#)
  23. J. DeSisto, R. O’Rourke, H. E. Jones, B. Pawlikowski, A. D. Malek, S. Bonney, F. Guimiot, K. L. Jones, J. A. Siegenthaler, Single-cell transcriptomic analyses of the developing meninges reveal meningeal fibroblast diversity and function. *Dev. Cell* **54**, 43–59.e4 (2020). [doi:10.1016/j.devcel.2020.06.009](https://doi.org/10.1016/j.devcel.2020.06.009) [Medline](#)
  24. J. Derk, H. E. Jones, C. Como, B. Pawlikowski, J. A. Siegenthaler, Living on the edge of the CNS: Meninges cell diversity in health and disease. *Front. Cell. Neurosci.* **15**, 703944 (2021). [doi:10.3389/fncel.2021.703944](https://doi.org/10.3389/fncel.2021.703944) [Medline](#)
  25. M. M. Mortazavi, S. A. Quadri, M. A. Khan, A. Gustin, S. S. Suriya, T. Hassanzadeh, K. M. Fahimdanesh, F. H. Adl, S. A. Fard, M. A. Taqi, I. Armstrong, B. A. Martin, R. S. Tubbs,

- Subarachnoid trabeculae: A comprehensive review of their embryology, histology, morphology, and surgical significance. *World Neurosurg.* **111**, 279–290 (2018). [doi:10.1016/j.wneu.2017.12.041](https://doi.org/10.1016/j.wneu.2017.12.041) [Medline](#)
26. S. E. Mutsaers, F. J. Pixley, C. M. Prêle, G. F. Hoyne, Mesothelial cells regulate immune responses in health and disease: Role for immunotherapy in malignant mesothelioma. *Curr. Opin. Immunol.* **64**, 88–109 (2020). [doi:10.1016/j.coi.2020.04.005](https://doi.org/10.1016/j.coi.2020.04.005) [Medline](#)
27. B. A. Hills, J. R. Burke, K. Thomas, Surfactant barrier lining peritoneal mesothelium: Lubricant and release agent. *Perit. Dial. Int.* **18**, 157–165 (1998). [doi:10.1177/089686089801800203](https://doi.org/10.1177/089686089801800203) [Medline](#)
28. A. Jayatilaka, Arachnoid granulations and arachnoid villi in mammals. *Ceylon J. Med. Sci.* **18**, 25–30 (1969).
29. D. G. Potts, V. Deonarine, Effect of positional changes and jugular vein compression on the pressure gradient across the arachnoid villi and granulations of the dog. *J. Neurosurg.* **38**, 722–728 (1973). [doi:10.3171/jns.1973.38.6.0722](https://doi.org/10.3171/jns.1973.38.6.0722) [Medline](#)
30. K. Suzuki, T. Kimura, H. Shinoda, G. Bai, M. J. Daniels, Y. Arai, M. Nakano, T. Nagai, Five colour variants of bright luminescent protein for real-time multicolour bioimaging. *Nat. Commun.* **7**, 13718 (2016). [doi:10.1038/ncomms13718](https://doi.org/10.1038/ncomms13718) [Medline](#)
31. Y. Su, J. R. Walker, Y. Park, T. P. Smith, L. X. Liu, M. P. Hall, L. Labanieh, R. Hurst, D. C. Wang, L. P. Encell, N. Kim, F. Zhang, M. A. Kay, K. M. Casey, R. G. Majzner, J. R. Cochran, C. L. Mackall, T. A. Kirkland, M. Z. Lin, Novel NanoLuc substrates enable bright two-population bioluminescence imaging in animals. *Nat. Methods* **17**, 852–860 (2020). [doi:10.1038/s41592-020-0889-6](https://doi.org/10.1038/s41592-020-0889-6) [Medline](#)
32. M. P. Hall, J. Unch, B. F. Binkowski, M. P. Valley, B. L. Butler, M. G. Wood, P. Otto, K. Zimmerman, G. Vidugiris, T. Machleidt, M. B. Robers, H. A. Benink, C. T. Eggers, M. R. Slater, P. L. Meisenheimer, D. H. Klaubert, F. Fan, L. P. Encell, K. V. Wood, Engineered luciferase reporter from a deep sea shrimp utilizing a novel imidazopyrazinone substrate. *ACS Chem. Biol.* **7**, 1848–1857 (2012). [doi:10.1021/cb3002478](https://doi.org/10.1021/cb3002478) [Medline](#)
33. J. Rustenhoven, A. Drieu, T. Mamuladze, K. A. de Lima, T. Dykstra, M. Wall, Z. Papadopoulos, M. Kanamori, A. F. Salvador, W. Baker, M. Lemieux, S. Da Mesquita, A. Cugurra, J. Fitzpatrick, S. Sviben, R. Kossina, P. Bayguinov, R. R. Townsend, Q. Zhang, P. Erdmann-Gilmore, I. Smirnov, M.-B. Lopes, J. Herz, J. Kipnis, Functional characterization of the dural sinuses as a neuroimmune interface. *Cell* **184**, 1000–1016.e27 (2021). [doi:10.1016/j.cell.2020.12.040](https://doi.org/10.1016/j.cell.2020.12.040) [Medline](#)
34. P. Mastorakos, D. McGavern, The anatomy and immunology of vasculature in the central nervous system. *Sci. Immunol.* **4**, eaav0492 (2019). [doi:10.1126/sciimmunol.aav0492](https://doi.org/10.1126/sciimmunol.aav0492) [Medline](#)
35. H. Baatz, M. Steinbauer, A. G. Harris, F. Krombach, Kinetics of white blood cell staining by intravascular administration of rhodamine 6G. *Int. J. Microcirc. Clin. Exp.* **15**, 85–91 (1995). [doi:10.1159/000178955](https://doi.org/10.1159/000178955) [Medline](#)
36. A. Merlini, M. Haberl, J. Strauß, L. Hildebrand, N. Genc, J. Franz, D. Chilov, K. Alitalo, C. Flügel-Koch, C. Stadelmann, A. Flügel, F. Odoardi, Distinct roles of the meningeal

- layers in CNS autoimmunity. *Nat. Neurosci.* **25**, 887–899 (2022). [doi:10.1038/s41593-022-01108-3](https://doi.org/10.1038/s41593-022-01108-3) [Medline](#)
37. A. Louveau, B. A. Plog, S. Antila, K. Alitalo, M. Nedergaard, J. Kipnis, Understanding the functions and relationships of the glymphatic system and meningeal lymphatics. *J. Clin. Invest.* **127**, 3210–3219 (2017). [doi:10.1172/JCI90603](https://doi.org/10.1172/JCI90603) [Medline](#)
38. S. Da Mesquita, Z. Fu, J. Kipnis, The meningeal lymphatic system: A new player in neurophysiology. *Neuron* **100**, 375–388 (2018). [doi:10.1016/j.neuron.2018.09.022](https://doi.org/10.1016/j.neuron.2018.09.022) [Medline](#)
39. Z. Xu, N. Xiao, Y. Chen, H. Huang, C. Marshall, J. Gao, Z. Cai, T. Wu, G. Hu, M. Xiao, Deletion of aquaporin-4 in APP/PS1 mice exacerbates brain A $\beta$  accumulation and memory deficits. *Mol. Neurodegener.* **10**, 58 (2015). [doi:10.1186/s13024-015-0056-1](https://doi.org/10.1186/s13024-015-0056-1) [Medline](#)
40. L. Wang, Y. Zhang, Y. Zhao, C. Marshall, T. Wu, M. Xiao, Deep cervical lymph node ligation aggravates AD-like pathology of APP/PS1 mice. *Brain Pathol.* **29**, 176–192 (2019). [doi:10.1111/bpa.12656](https://doi.org/10.1111/bpa.12656) [Medline](#)
41. A. Z. Mohamed, P. Cumming, J. Götz, F. Nasrallah; Department of Defense Alzheimer's Disease Neuroimaging Initiative, Tauopathy in veterans with long-term posttraumatic stress disorder and traumatic brain injury. *Eur. J. Nucl. Med. Mol. Imaging* **46**, 1139–1151 (2019). [doi:10.1007/s00259-018-4241-7](https://doi.org/10.1007/s00259-018-4241-7) [Medline](#)
42. J. D. Flatt, P. Gilsanz, C. P. Quesenberry Jr., K. B. Albers, R. A. Whitmer, Post-traumatic stress disorder and risk of dementia among members of a health care delivery system. *Alzheimers Dement.* **14**, 28–34 (2018). [doi:10.1016/j.jalz.2017.04.014](https://doi.org/10.1016/j.jalz.2017.04.014) [Medline](#)
43. S. Brioschi, W.-L. Wang, V. Peng, M. Wang, I. Shchukina, Z. J. Greenberg, J. K. Bando, N. Jaeger, R. S. Czepielewski, A. Swain, D. A. Mogilenko, W. L. Beatty, P. Bayguinov, J. A. J. Fitzpatrick, L. G. Schuettepelz, C. C. Fronick, I. Smirnov, J. Kipnis, V. S. Shapiro, G. F. Wu, S. Gilfillan, M. Cella, M. N. Artyomov, S. H. Kleinstejn, M. Colonna, Heterogeneity of meningeal B cells reveals a lymphopoietic niche at the CNS borders. *Science* **373**, eabf9277 (2021). [doi:10.1126/science.abf9277](https://doi.org/10.1126/science.abf9277) [Medline](#)
44. J. J. Iliff, M. J. Chen, B. A. Plog, D. M. Zeppenfeld, M. Soltero, L. Yang, I. Singh, R. Deane, M. Nedergaard, Impairment of glymphatic pathway function promotes tau pathology after traumatic brain injury. *J. Neurosci.* **34**, 16180–16193 (2014). [doi:10.1523/JNEUROSCI.3020-14.2014](https://doi.org/10.1523/JNEUROSCI.3020-14.2014) [Medline](#)
45. N. B. Pikor, A. Prat, A. Bar-Or, J. L. Gommerman, Meningeal tertiary lymphoid tissues and multiple sclerosis: A gathering place for diverse types of immune cells during CNS autoimmunity. *Front. Immunol.* **6**, 657 (2016). [Medline](#)
46. X. Han, M. Chen, F. Wang, M. Windrem, S. Wang, S. Shanz, Q. Xu, N. A. Oberheim, L. Bekar, S. Betstadt, A. J. Silva, T. Takano, S. A. Goldman, M. Nedergaard, Forebrain engraftment by human glial progenitor cells enhances synaptic plasticity and learning in adult mice. *Cell Stem Cell* **12**, 342–353 (2013). [doi:10.1016/j.stem.2012.12.015](https://doi.org/10.1016/j.stem.2012.12.015) [Medline](#)
47. H. Mestre, T. Du, A. M. Sweeney, G. Liu, A. J. Samson, W. Peng, K. N. Mortensen, F. F. Stæger, P. A. R. Bork, L. Bashford, E. R. Toro, J. Tithof, D. H. Kelley, J. H. Thomas, P. G. Hjorth, E. A. Martens, R. I. Mehta, O. Solis, P. Blinder, D. Kleinfeld, H. Hirase, Y.

- Mori, M. Nedergaard, Cerebrospinal fluid influx drives acute ischemic tissue swelling. *Science* **367**, eaax7171 (2020). [doi:10.1126/science.aax7171](https://doi.org/10.1126/science.aax7171) [Medline](#)
48. K. Møllgård, K. M. Dziegielewska, C. B. Holst, M. D. Habgood, N. R. Saunders, Brain barriers and functional interfaces with sequential appearance of ABC efflux transporters during human development. *Sci. Rep.* **7**, 11603 (2017). [doi:10.1038/s41598-017-11596-0](https://doi.org/10.1038/s41598-017-11596-0) [Medline](#)
49. L. Xie, H. Kang, Q. Xu, M. J. Chen, Y. Liao, M. Thiagarajan, J. O'Donnell, D. J. Christensen, C. Nicholson, J. J. Iliff, T. Takano, R. Deane, M. Nedergaard, Sleep drives metabolite clearance from the adult brain. *Science* **342**, 373–377 (2013). [doi:10.1126/science.1241224](https://doi.org/10.1126/science.1241224) [Medline](#)
50. L. M. Hablitz, V. Plá, M. Giannetto, H. S. Vinitsky, F. F. Stæger, T. Metcalfe, R. Nguyen, A. Benrais, M. Nedergaard, Circadian control of brain glymphatic and lymphatic fluid flow. *Nat. Commun.* **11**, 4411 (2020). [doi:10.1038/s41467-020-18115-2](https://doi.org/10.1038/s41467-020-18115-2) [Medline](#)
51. A. L. R. Xavier, N. L. Hauglund, S. von Holstein-Rathlou, Q. Li, S. Sanggaard, N. Lou, I. Lundgaard, M. Nedergaard, Cannula implantation into the cisterna magna of rodents. *J. Vis. Exp.* **2018**, 57378 (2018). [doi:10.3791/57378](https://doi.org/10.3791/57378) [Medline](#)
52. G. Liu, H. Mestre, A. M. Sweeney, Q. Sun, P. Weikop, T. Du, M. Nedergaard, Direct measurement of cerebrospinal fluid production in mice. *Cell Rep.* **33**, 108524 (2020). [doi:10.1016/j.celrep.2020.108524](https://doi.org/10.1016/j.celrep.2020.108524) [Medline](#)
53. A. François, F. Terro, N. Quellard, B. Fernandez, D. Chassaing, T. Janet, A. Rioux Bilan, M. Paccalin, G. Page, Impairment of autophagy in the central nervous system during lipopolysaccharide-induced inflammatory stress in mice. *Mol. Brain* **7**, 56 (2014). [doi:10.1186/s13041-014-0056-z](https://doi.org/10.1186/s13041-014-0056-z) [Medline](#)
54. J. Schindelin, I. Arganda-Carreras, E. Frise, V. Kaynig, M. Longair, T. Pietzsch, S. Preibisch, C. Rueden, S. Saalfeld, B. Schmid, J.-Y. Tinevez, D. J. White, V. Hartenstein, K. Eliceiri, P. Tomancak, A. Cardona, Fiji: An open-source platform for biological-image analysis. *Nat. Methods* **9**, 676–682 (2012). [doi:10.1038/nmeth.2019](https://doi.org/10.1038/nmeth.2019) [Medline](#)